


# Surface Exciton Polaritons: A Promising Mechanism for Refractive-Index Sensing

Yi Xu<sup>1,2,\*</sup>, Lin Wu,<sup>2</sup> and L.K. Ang<sup>1,†</sup>

<sup>1</sup>*SUTD-MIT International Design Centre & Science and Math Cluster, Singapore University of Technology and Design, 8 Somapah Road, Singapore 487372, Singapore*

<sup>2</sup>*Institute of High Performance Computing, Agency for Science, Technology and Research, 1 Fusionopolis Way, #16-16 Connexis, Singapore 138632, Singapore*

 (Received 9 April 2019; revised manuscript received 26 May 2019; published 15 August 2019)

Room-temperature surface exciton polaritons (SEPs) were successfully demonstrated recently by replacement of the metal thin film in the Kretschmann-Raether configuration of surface plasmon polaritons (SPPs) with a film of the J-aggregate cyanine dye 5,6-dichloro-2-[[5,6-dichloro-1-ethyl-3-(4-sulfobutyl)benzimidazol-2-ylidene]propenyl]-1-ethyl-3-(4-sulfobutyl)benzimidazolium hydroxide (TDBC). Compared with SPPs (i.e., photons coupled to highly mobile free electrons at the metal surface), the coupling of photons to less-mobile excitons supports stronger field confinement at the TDBC surface. This extraordinary field confinement of SEPs beyond SPPs motivated us to explore the feasibility of refractive-index (RI) sensing, in particular, surface RI sensing. We find that the bulk RI sensitivity of  $118^\circ$  ( $140^\circ$ ) per refractive-index unit (RIU) of the proposed SEP sensor in the RI range from 1.0 to 1.001 (from 1.33 to 1.36) for a gaseous analyte (an aqueous solution) is higher than that of a conventional gold-based SPP sensor [ $73^\circ$ /RIU ( $124^\circ$ /RIU)]. For surface RI sensing, the SEP sensor has both higher sensitivity and a higher figure of merit than the SPP sensor. These numerical results undoubtedly reveal SEPs to be a promising mechanism for sensing.

DOI: [10.1103/PhysRevApplied.12.024029](https://doi.org/10.1103/PhysRevApplied.12.024029)

## I. INTRODUCTION

A surface exciton polariton (SEP) is an elementary excitation resulting from the coupling of photons to excitons at the surface of a crystal. SEPs have been observed experimentally in various inorganic semiconductors, including ZnO [1,2], CuBr [3,4], CuCl [4], and ZnSe [5]. However, successful observation of SEPs in these media requires cryogenic temperature, which limits their practical applications. This limitation is because the excitons in these inorganic semiconductors are Wannier-Mott excitons, which have low binding energy (approximately 10 meV) below the thermal energy at room temperature (25 meV) [6]. In contrast, excitons in organic crystals are Frenkel excitons, with much higher binding energy (approximately 1 eV) [6], which allows the observation of SEPs in organic crystals at room temperature. SEPs in organic materials were experimentally demonstrated at room temperature in the 1970s [7–10]. The SEPs were observed in the Otto configuration, where the metal film was replaced with an organic crystalline solid. In these experiments, a specific

crystal face was required for the observation of SEPs. In 2017, by replacement of the metal thin film in the traditional Kretschmann-Raether configuration [11] with an organic noncrystalline medium, 5,6-dichloro-2-[[5,6-dichloro-1-ethyl-3-(4-sulfobutyl)benzimidazol-2-ylidene]propenyl]-1-ethyl-3-(4-sulfobutyl)benzimidazolium hydroxide (TDBC), Takatori *et al.* [12] experimentally observed SEPs under 532-nm illumination at room temperature. The observation of SEPs at room temperature opens the door to practical applications (e.g., optical sensing).

Optical sensing has been widely used in environmental monitoring, immunoassays, medical diagnostics, and food safety [13–26]. One of the most-popular sensing mechanisms is based on surface plasmon resonance (SPR) [27,28], including propagating surface plasmon polaritons (SPPs) and localized SPR. Similarly to a SEP, a SPP is also an elementary excitation, which results from the coupling of photons to plasmons (i.e., free electrons). A classic SPP sensing structure is based on the Kretschmann-Raether configuration, prism-metal-analyte [11,26], which is similar to the structure (prism-TDBC-air) supporting SEPs [12]. Considering the similarities and differences between SPPs and SEPs, we are curious to know whether it is possible to use SEPs for sensing applications. What will be the

\*[yi\\_xu@mymail.sutd.edu.sg](mailto:yi_xu@mymail.sutd.edu.sg)

†[ricky\\_ang@sutd.edu.sg](mailto:ricky_ang@sutd.edu.sg)

sensing performance of a SEP sensor as compared with a conventional SPP sensor? Addressing these questions is of great importance for the practical application of SEPs.

In this work, we systematically study two types of SEP sensors based on a prism-TDBC-analyte structure. The first type is bulk refractive-index (RI) sensing; for example, to be used as a gas sensor in the environmental RI range of 1.0–1.001 [29–31]. For this case, typically, the change of RI occurs all around the environment. The second type is surface RI sensing, which is more relevant to biosensing [32–34], which is usually conducted in an aqueous solution with RI around 1.33. Here, the biomolecules are adsorbed on the sensor surface and RI variations occur only within a very small space close to the sensor surface.

In our study, we benchmark the proposed SEP sensors against conventional SPP sensors.

## II. DESIGN CONSIDERATION AND THEORETICAL MODEL

To excite SEPs, the traditional SPR structure, a Kretschmann-Raether configuration [11], is used, where the surface-plasmon-supporting metal film is replaced by a TDBC film, as shown in Fig. 1(a). The TDBC is deposited on a thin glass substrate, and the glass substrate is attached to a glass prism. The glass prism can be made of BK7 glass, SF11 glass, or a chalcogenide  $\text{Ge}_{20}\text{Ga}_5\text{Sb}_{10}\text{S}_{65}$  (2S2G) glass, and their RIs under 532-nm illumination are

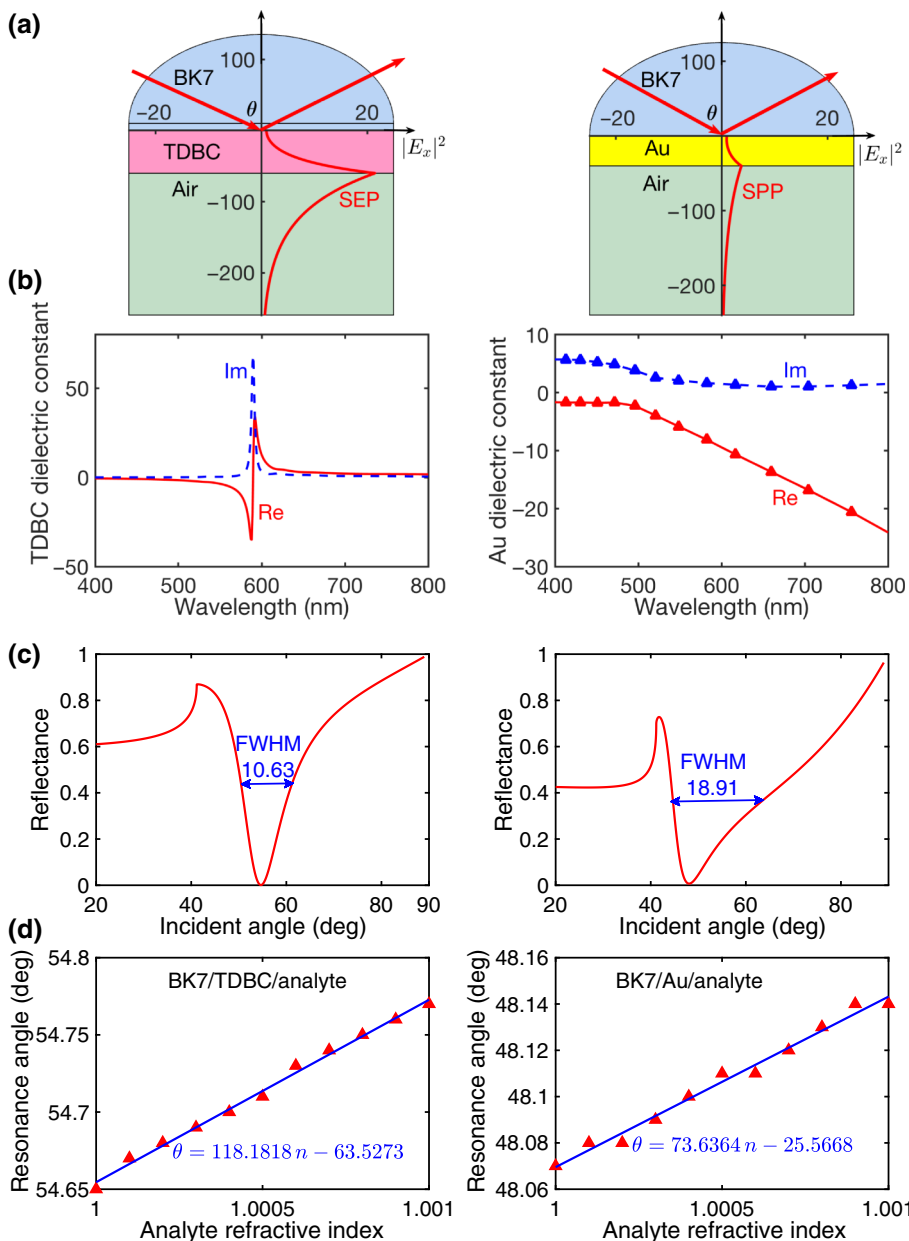


FIG. 1. Comparison between SEP and SPP gas sensors under 532-nm illumination. (a) Sensor structure with the density distribution of the electric field  $x$  component at the resonance angle. (b) Dielectric constant for TDBC and Au. (c) Reflectance–incident-angle curve. (d) Variation of the resonance angle with analyte RI. The thicknesses of the TDBC and Au films are 60 and 40 nm, respectively.

1.5195, 1.7948, and 2.4365, respectively [22–24,35]. The dielectric constant of the TDBC film is calculated by the following relation [12]:

$$\varepsilon(\omega) = \sum_{j=1}^5 \frac{\omega_{pj}^2}{\omega_{0j}^2 - \omega^2 - i\gamma_j \omega}, \quad (1)$$

where  $\omega_{p1} = 4340 \text{ cm}^{-1}$ ,  $\omega_{p2} = 4383 \text{ cm}^{-1}$ ,  $\omega_{p3} = 3511 \text{ cm}^{-1}$ ,  $\omega_{p4} = 11830 \text{ cm}^{-1}$ ,  $\omega_{p5} = 1621 \text{ cm}^{-1}$ ,  $\omega_{01} = 13570 \text{ cm}^{-1}$ ,  $\omega_{02} = 15330 \text{ cm}^{-1}$ ,  $\omega_{03} = 16140 \text{ cm}^{-1}$ ,  $\omega_{04} = 16960 \text{ cm}^{-1}$ ,  $\omega_{05} = 1810 \text{ cm}^{-1}$ ,  $\gamma_1 = 2409 \text{ cm}^{-1}$ ,  $\gamma_2 = 1352 \text{ cm}^{-1}$ ,  $\gamma_3 = 565.5 \text{ cm}^{-1}$ ,  $\gamma_4 = 117.3 \text{ cm}^{-1}$ ,  $\gamma_5 = 561.6 \text{ cm}^{-1}$ , and  $\omega = 1/\lambda$  is the wave number in reciprocal centimeters. The real and imaginary parts of the calculated dielectric constant of the TDBC film as a function of illumination wavelength are shown in Fig. 1(b). The TDBC film supports SEPs in the illumination wavelength range from 463 to 589 nm, where the complex dielectric constant of the TDBC film has a real part less than  $-1$  [12]. For comparison, the measured complex dielectric constant of a Au film [36] is also presented in Fig. 1(b), which shows that the Au film can support SPPs beyond an illumination wavelength of 589 nm.

For  $p$ -polarized light incident on the prism-coupled SEP structure, the reflection coefficient ( $r_p$ ) is obtained as

$$r_p = \frac{(\cos \beta_2 - iq_3 \sin \beta_2/q_2)q_1 - (q_3 \cos \beta_2 - iq_2 \sin \beta_2)}{(\cos \beta_2 - iq_3 \sin \beta_2/q_2)q_1 + (q_3 \cos \beta_2 - iq_2 \sin \beta_2)}, \quad (2)$$

where

$$\beta_2 = \frac{2\pi d_2}{\lambda} (n_2^2 - n_1^2 \sin^2 \theta_1)^{1/2} \quad (3)$$

and

$$q_j = \frac{(n_j^2 - n_1^2 \sin^2 \theta_1)^{1/2}}{n_j^2} \quad (j = 1, 2, 3). \quad (4)$$

Here  $n_1$ ,  $n_2$ , and  $n_3$  are the RIs of the prism, TDBC, and analyte, respectively,  $\lambda$  is the wavelength of incident light,

and  $\theta_1 = \theta$  is the incident angle at the base of the prism (see Fig. 1). The reflectance  $R_p$  is given by  $R_p = |r_p|^2$ .

For sensing applications, a RI variation of the analyte  $\Delta n_3$  will cause a change in the reflectivity and the resonance angle ( $\Delta\theta_{\text{res}}$ ) of the SEP. Thus, the angular sensitivity of a SEP sensor is defined as

$$S = \frac{\Delta\theta_{\text{res}}}{\Delta n_3}. \quad (5)$$

Another parameter to describe the sensor performance is the figure of merit (FOM), which is defined as  $\text{FOM} = S/\text{FWHM}$ , where FWHM is the full width at half maximum, which describes the width of the reflectance–incident-angle curve. Normally, higher sensitivity  $S$  and a larger FOM are desirable for an optical sensor.

### III. RESULTS AND DISCUSSION

The analyte that directly contacts the TDBC film is a gaseous analyte or an aqueous solution. In this section, we discuss the applications of SEPs in gas sensing and biosensing. The incident light is  $p$  polarized with a wavelength of 532 nm. The complex dielectric constants of TDBC film and Au film under 532-nm illumination are  $-2.5886 + 0.3748i$  and  $-4.6811 + 2.4266i$ , respectively.

#### A. Gas sensing

The BK7-TDBC-air structure is proposed to excite SEPs, as shown in Fig. 1(a). A resonance dip in the reflectance–incident-angle curve is observed [see Fig. 1(c)] when the SEPs are excited. Here the thickness of TDBC is 60 nm, which gives the deepest resonance dip, as shown in Fig. 2(a). At the resonance angle, the electric field is strongest at the interface between the TDBC film and air, and exponentially decays into air [see Fig. 1(a)]. This property of SEPs is similar to that of SPPs [37], which are very sensitive to ambient RI changes. This in turn makes SEPs a promising candidate for sensing applications. For example, this proposed SEP structure can be used for gas sensing. The resonance angle as a function of the gas (i.e., the analyte) RI in the range from 1.0 to 1.001 is shown in the Fig.

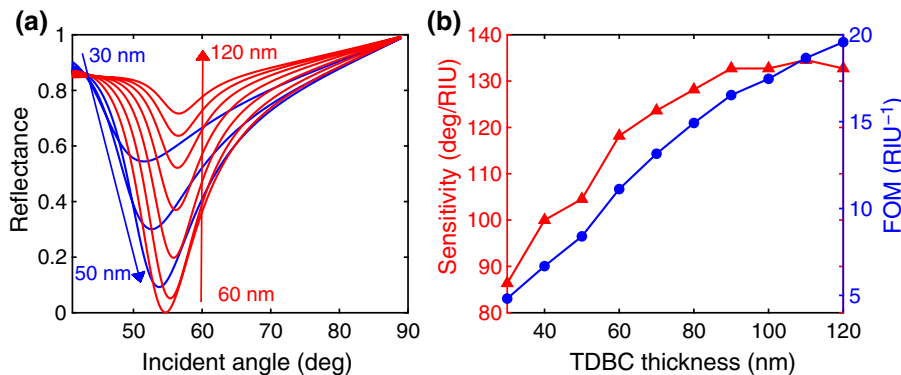


FIG. 2. (a) Reflectance as a function of incident angle for the BK7-TDBC-air structure with different thicknesses of the TDBC film. (b) Variation of the sensitivity and FOM with the thickness of the TDBC film.

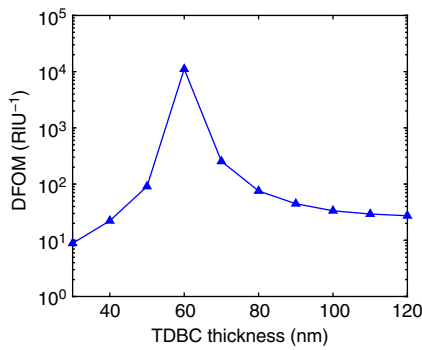


FIG. 3. FOM as a function of thickness of the TDBC film for the BK7-TDBC-air structure.

1(d). It is found that the resonance angle increases with the analyte RI, and a RI sensitivity of  $118.18^\circ$  per refractive-index unit (RIU) is achieved. For comparison, the electric field distribution, reflectance–incident-angle curve, and RI sensitivity of a conventional SPP sensor (BK7-Au(40 nm)-air) are also shown in Fig. 1. Our choice of a 40-nm-thick Au film results in the reflectance of the SPP sensor being close to zero at the resonance angle. It is worth noting that the selected thickness of the Au (or TDBC) film is comparable to the skin depth [38] of Au (TDBC) under 532 nm illumination, which is about 38 nm (52 nm).

The electric field strength  $|E_x|^2$  at the Au-air interface for a SPP sensor (typically around 2–4 for a 30–60-nm-thick Au film; see Fig. S1 in Supplemental Material [39]) is generally smaller than that at the TDBC-air interface for a SEP sensor (typically around 11–21 for

a 30–80-nm-thick TDBC film; see Fig. S1 in Supplemental Material [39]). One typical example is shown in Fig. 1(a). Compared with a SPP, a SEP is a result of the coupling of photons to less-mobile excitons [40], which allows stronger field confinement at the TDBC surface. However, a SPP sensor typically has a greater penetration depth (70–81 nm) than a SEP sensor (54–66 nm) (see Fig. S1 in Supplemental Material [39]). In the case of Fig. 1(a), it is approximately 80 nm (SPP) versus approximately 57 nm (SEP). Here the penetration depth is defined as the depth in the analyte where the maximum amplitude of the electric field decreases by a factor of  $1/e$ . In addition, the Au-based SPP sensor exhibits a broader reflectance–incident-angle curve than does the TDBC-based SEP sensor. The FWHM for the SPP sensor is  $18.91^\circ$ , while it is  $10.63^\circ$  for the SEP sensor [see Fig. 1(c)]. The SPP sensor exhibits a RI sensitivity of  $73.64^\circ/\text{RIU}$ , which is about 62.31% of the sensitivity for the SEP-based gas sensor. The FOM of the SEP sensor is  $11.12 \text{ RIU}^{-1}$ , about 2.86 times higher than that of the SPP sensor (FOM  $3.89 \text{ RIU}^{-1}$ ). This reveals that a SEP sensor is a promising alternative for sensing technology with higher sensitivity and larger FOM than a conventional SPP sensor.

The sensitivity of the proposed SEP gas sensor is strongly affected by the thickness of the TDBC film. Figure 2(a) illustrates the variation of the reflectance with the incident angle for a SEP gas sensor with different thicknesses of the TDBC film. The resonance angle moves to a higher angle of incidence. The resonance depth  $R_{\text{res}}$  (i.e., the reflectance at the resonance angle) is greatly dependent on the TDBC thickness, which is related to the SEP excitation. The resonance depth  $R_{\text{res}}$  first decreases and

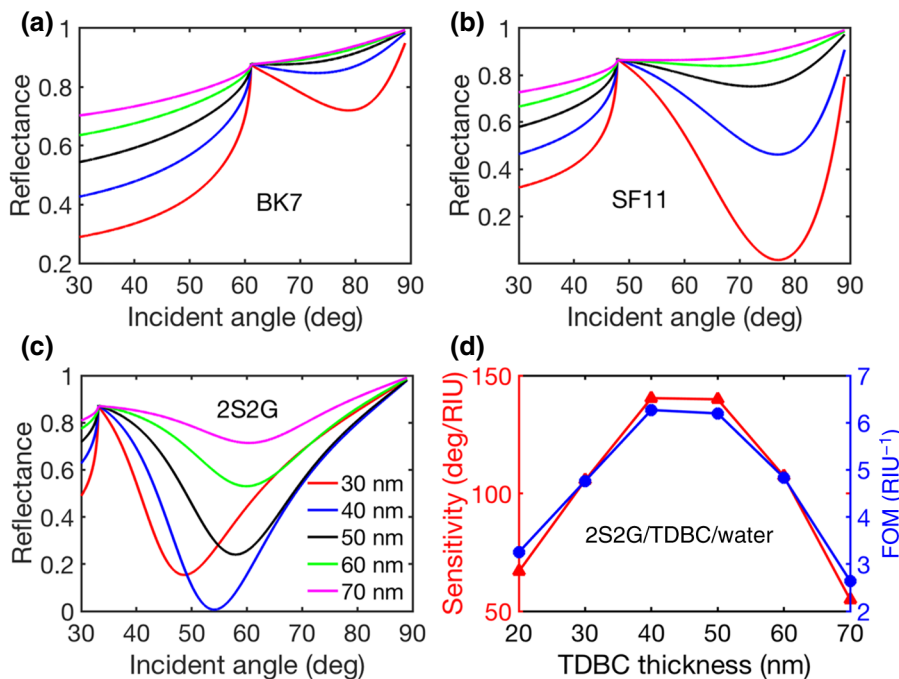


FIG. 4. Reflectance–incident-angle curves for the prism-TDBC-water structure with different thicknesses of the TDBC film: (a) BK7, (b) SF11, and (c) 2S2G. (d) The sensitivity and FOM for the SEP biosensor with the 2S2G-TDBC-water structure.

then increases with the TDBC thickness. The deepest resonance dip is found with the 60-nm-thick TDBC film, where the excitation of SEPs is strongest. A thick TDBC film (e.g., 120-nm TDBC film) has a much-shallower reflectance–incident-angle curve, at which the incident energy absorbed by the TDBC film is insufficient to excite a strong SEP. The TDBC-thickness-dependent sensitivity and FOM are shown in Fig. 2(b). In general, the sensitivity increases with the thickness of the TDBC film in the range from 30 to 120 nm in spite of a plateau (90 and 100 nm) and one drop (from 110 to 120 nm). The FOM monotonically increases with the TDBC thickness. Although SEP sensors with a thicker TDBC film have greater sensitivity and FOM, the reflectance–incident-angle curve is much shallower as compared with the 60-nm-thick-TDBC case. For example, the SEP gas sensor with a 120-nm TDBC film exhibits a RI sensitivity of  $132.7^\circ/\text{RIU}$ , whereas its resonance depth  $R_{\text{res}} = 0.7167$  with an ambient RI of 1.0. This shallow reflectance–incident-angle curve will limit the applications of the SEP sensor. Here we define another parameter, DFOM (dip to FoM), as  $\text{DFOM} = \text{FOM}/R_{\text{res}}$  to include the effect of resonance depth  $R_{\text{res}}$ . Thus, a larger DFOM is desirable for a SEP sensor. DFOM, includes

the RI sensitivity, FOM, and resonance depth. DFOM has a maximum value with a TDBC thickness of 60 nm, as shown in Fig. 3. Therefore, a 60-nm TDBC film is the best choice when the sensitivity, FOM, and resonance depth are taken into consideration. In addition, the SEP gas sensor has higher sensitivity and a larger FOM than the SPP gas sensor for a film (TDBC or Au) thickness from 30 to 120 nm (see Fig. S1 in Supplemental Material [39]).

## B. Biosensing

We have discussed gas sensing with BK7-TDBC-gas structure. But would this structure operate in a watery environment? To address this question, the reflectance–incident-angle curves for the BK7-TDBC-water structure (RI approximately 1.33) are plotted in Fig. 4(a). The BK7-based sensor exhibits a very shallow resonance dip and a resonance angle of approximately  $80^\circ$  with a 30-nm TDBC film. For a thicker TDBC film, it is hard to excite the SEPs. By replacing the BK7 prism with an SF11 prism, we achieve a stronger excitation of the SEPs with the 30-nm TDBC film, as shown in Fig. 4(b). A resonance depth  $R_{\text{res}} = 0.0137$  is obtained although the resonance angle

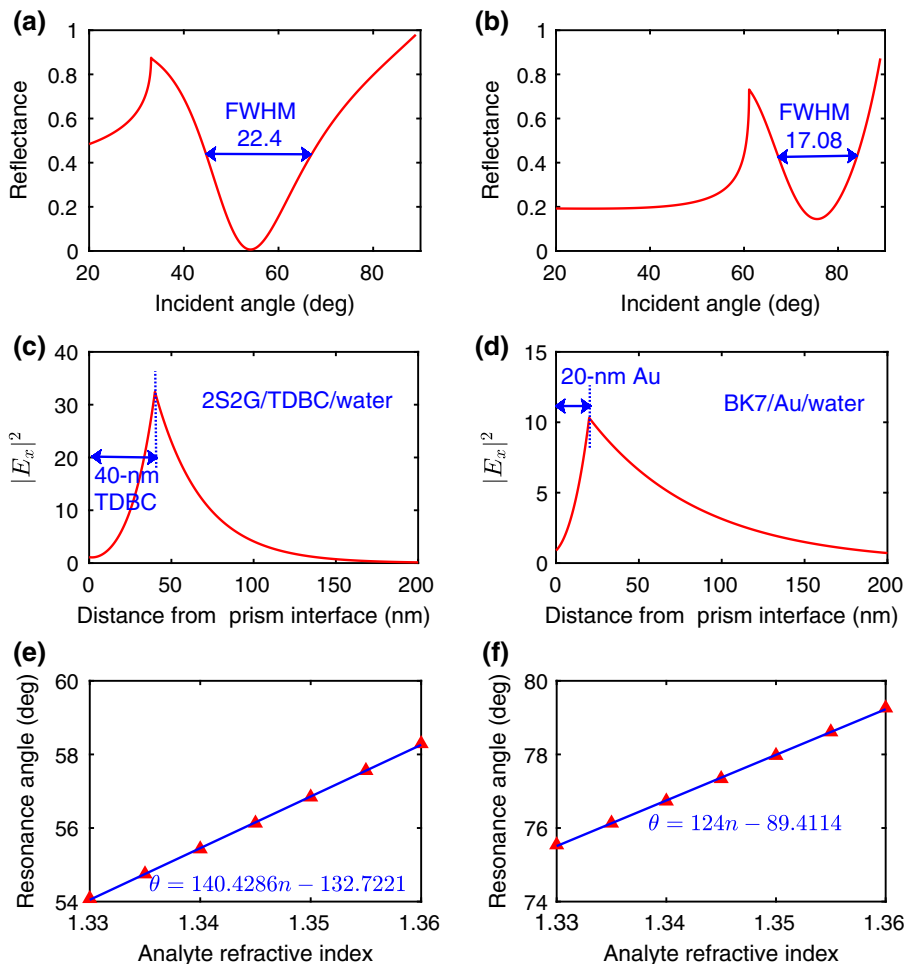


FIG. 5. Comparison between SEP and SPP biosensors under 532-nm illumination. Reflectance–incident-angle curve: (a) SEP biosensor and (b) SPP biosensor. The density distribution of the electric field  $x$  component at the resonance angle: (c) SEP biosensor and (d) SPP biosensor. Variation of the resonance angle with analyte RI: (e) SEP biosensor and (f) SPP biosensor. The thicknesses of the TDBC and Au films are 40 and 20 nm, respectively.

is approximately  $77^\circ$ . In contrast, the 2S2G-based sensor with a 40-nm TDBC film has a minimum reflectance of 0.0066 at the resonance angle of  $54.08^\circ$  [see Fig. 4(c)]. From comparison of the reflectance–incident-angle curves for the three prisms, it is found that the 2S2G prism is more specifically suited to biosensing. Therefore, in the following, we focus on the 2S2G-TDBC-analyte structure and discuss its sensor performance in a watery environment.

For biosensing applications, the analyte is an aqueous solution, and the RI range we consider is 1.33–1.36. The TDBC-thickness-dependent RI sensitivity and FOM for the SEP biosensor with the 2S2G-TDBC-water structure are shown in Fig. 4(d). The RI sensitivity first increases and then decreases with the TDBC thickness, which is different from the behavior for the SEP-based gas sensor [see Fig. 2(b)]. The maximum sensitivity of  $140.43^\circ/\text{RIU}$  is achieved with the 40-nm TDBC film, while the 50-nm-thick-TDBC-based SEP sensor has a similar sensitivity of  $139.93^\circ/\text{RIU}$ . The FOM exhibits the same behavior as that of the RI sensitivity, and the maximum FOM of  $6.27 \text{ RIU}^{-1}$  is obtained with the 40-nm TDBC film. In addition, the parameter DFOM also suggests the SEP biosensor with a 40-nm TDBC film has the best sensing ability.

A comparison of the SEP-based biosensor and the SPP-based biosensor is presented in Fig. 5. Here the structure of the SEP-based biosensor is 2S2G-TDBC(40 nm)-water, while the structure of the SPP biosensor is BK7-Au(20 nm)-water. This choice of SEP-biosensor (SPP-biosensor) structure provides the maximum RI sensitivity for the SEP-based (SPP-based) biosensor (see Fig. 4 and Figs. S2–S4 in Supplemental Material [39]). The reflectance–incident-angle curves for the SEP and SPP biosensors are shown in Figs. 5(a) and 5(b), respectively. The SEP biosensor has a smaller resonance depth but a larger FWHM than the SPP biosensor. The electric field strength at the TDBC-water interface for the SEP biosensor is much higher than that at the Au-water interface for the SPP biosensor [see Figs. 5(c) and 5(d)]. However, the electric field decays more quickly in water for the SEP biosensor as compared with the SPP biosensor. The penetration depth of the SEP biosensor is approximately 29 nm, whereas it is approximately 67 nm for the SPP biosensor.

The variation of resonance angle with the RI of the aqueous solution for the SEP biosensor is shown in Fig. 5(e). The resonance angle increases with the analyte RI, and a RI sensitivity of  $140.43^\circ/\text{RIU}$  is achieved. The SPP biosensor with the BK7-Au(20 nm)-water structure exhibits a RI sensitivity of  $124^\circ/\text{RIU}$ , which is less than that of the SEP biosensor. The FOM of the SPP biosensor is  $7.26 \text{ RIU}^{-1}$ , which is higher than that of the SEP biosensor ( $6.27 \text{ RIU}^{-1}$ ). Therefore, the SEP is also a promising technology for biosensing applications.

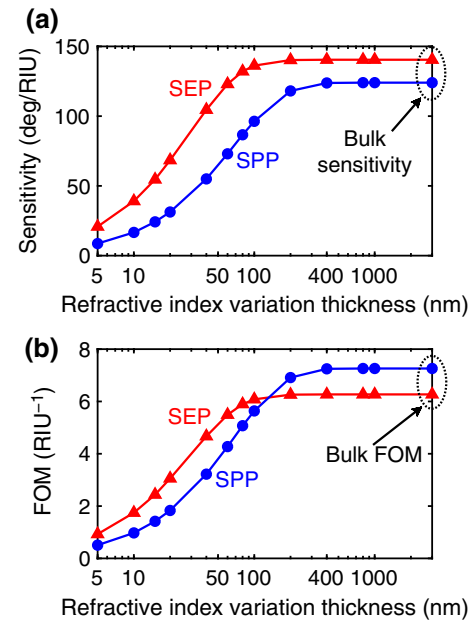


FIG. 6. (a) Sensitivity and (b) FOM for SEP and SPP biosensors as a function of the RI variation thickness.

The RI variations in the SEP and SPP biosensors occur within the whole analyte, which refers to the bulk RI variations. Accordingly, the sensitivity and FOM related to the bulk RI variations are known as “bulk sensitivity” and “bulk FOM.” Besides the bulk sensing, the RI change occurs within a very small space (i.e., finite thickness in the analyte) close to the surface of the biosensor and is called “surface RI variations.” The RI sensitivities and figures of merit for the SEP and SPP biosensors as a function of the RI variation thickness are shown in Fig. 6. The surface RI sensitivity (surface FOM) is smaller than the bulk RI sensitivity (bulk FOM). For example, within the RI variation occurs in a thickness of 5 nm, the SEP biosensor exhibits a surface RI sensitivity of  $20.79^\circ/\text{RIU}$ , 14.8% of the bulk RI sensitivity of the SEP biosensor ( $140.43^\circ/\text{RIU}$ ). The surface FOM is  $0.93 \text{ RIU}^{-1}$ , whereas the bulk FOM of the SEP biosensor is  $6.27 \text{ RIU}^{-1}$ . The surface RI sensitivity (FOM) increases with the RI variation thickness, and transforms to the bulk RI sensitivity (FOM) for a large-enough RI variation thickness, as shown in Fig. 6. The SPP biosensor has lower RI sensitivity than the SEP biosensor for both surface and bulk sensing. The SEP biosensor exhibits a larger surface FOM but a smaller bulk FOM than the SPP biosensor.

#### IV. CONCLUSION

In this work, a room-temperature SEP sensor is explored by our replacing the metal film in the Kretschmann-Raether configuration of a conventional SPP sensor with TDBC film. The excitation of the SEP results in a strong electric field at the interface of TDBC and the analyte, and exponentially decays into the analyte, and

is sensitive to the analyte RI variations. The proposed SEP gas sensor exhibits significant superiority in terms of RI sensitivity over the conventional Au-based SPP gas sensor. The bulk sensitivity of  $118.18^\circ/\text{RIU}$  with a bulk FOM of  $11.12 \text{ RIU}^{-1}$  is achieved in the RI range from 1.0 to 1.001 for the SEP gas sensor, while the traditional Au-based SPP gas sensor exhibits a bulk RI sensitivity of  $73.64^\circ/\text{RIU}$  with a bulk FOM of  $3.89 \text{ RIU}^{-1}$ . The SEP based biosensor with the 2S2G-TDBC-analyte structure has higher bulk RI sensitivity ( $140.43^\circ/\text{RIU}$ ) but a smaller bulk FOM ( $6.27 \text{ RIU}^{-1}$ ) than the SPP biosensor with the BK7-Au-analyte structure (sensitivity  $124^\circ/\text{RIU}$ , FOM  $7.26 \text{ RIU}^{-1}$ ) in the RI range from 1.33 to 1.36. In terms of surface RI sensing, both the surface RI sensitivity and the surface FOM of the SEP sensor exceed those of the SPP biosensor. With the excellent sensor performance, the proposed SEP-based sensor may provide an alternative to previous sensing technology based on SPPs. It should be noted that the TDBC film fabricated with a spin-coating technique has a larger surface roughness as compared with Au film in SPP sensors. Thus, the thickness control of TDBC film is an important factor impacting the sensing ability of the SEP sensor. In addition, organic materials, such as polymers, have been widely used in SPP sensors to capture biomolecules, ions, and gases, aiming to increase the selectivity, stability, and sensitivity [41–46]. Therefore, a SEP sensor with organic materials (e.g., TDBC) may have high affinity and selectivity for the target molecules.

### ACKNOWLEDGMENTS

Y.X. and L.K.A. acknowledge the Singapore A\*STAR AME IRG (A1783c0011), U.S. Air Force Office of Scientific Research through the Asian Office of Aerospace Research and Development under Grant No. FA2386-17-1-4020, and Singapore Ministry of Education Tier 2 Grant No. 2018-T2-1-007. The Institute of High Performance Computing acknowledges financial support from the National Research Foundation Singapore (Grants No. NRF2017-NRF-NSFC002-015 and No. NRF2016-NRF-ANR002).

- 
- [1] J. Lagaio and B. Fischer, Experimental Observation of Surface Exciton Polaritons, *Phys. Rev. Lett.* **36**, 680 (1976).
  - [2] I. Hirabayashi, Y. Tokura, and T. Koda, Surface exciton polariton in ZnO, *J. Phys. Soc. Jpn.* **51**, 2934 (1982).
  - [3] I. Hirabayashi, Y. Tokura, J. Murata, and Y. Kaneko, Surface exciton-polariton in CuBr, *J. Phys. Soc. Jpn.* **40**, 1215 (1976).
  - [4] I. Hirabayashi, T. Koda, Y. Tokura, J. Murata, and Y. Kaneko, Surface exciton polariton in CuCl and CuBr, *J. Phys. Soc. Jpn.* **43**, 173 (1977).

- [5] Y. Tokura, T. Koda, I. Hirabayashi, and S. Nakada, Surface exciton polariton in ZnSe, *J. Phys. Soc. Jpn.* **50**, 145 (1981).
- [6] S. Kéna-Cohen and S. Forrest, Room-temperature polariton lasing in an organic single-crystal microcavity, *Nat. Photonics* **4**, 371 (2010).
- [7] A. Brillante, I. Pockrand, M. Philpott, and J. Swalen, Experimental observation of exciton surface polaritons on a polymerized diacetylene crystal, *Chem. Phys. Lett.* **57**, 395 (1978).
- [8] I. Pockrand, A. Brillante, M. Philpott, and J. Swalen, Observation of exciton surface polaritons at room temperature, *Opt. Commun.* **27**, 91 (1978).
- [9] A. Brillante, M. Philpott, and I. Pockrand, Experimental and theoretical study of exciton surface polaritons on organic crystals. I. (010) face of TCNQ<sup>o</sup> single crystals, *J. Chem. Phys.* **70**, 5739 (1979).
- [10] M. R. Philpott, I. Pockrand, A. Brillante, and J. Swalen, Experimental and theoretical study of exciton surface polaritons on organic crystals. II. Highly reflecting faces of CTIP and PTS, *J. Chem. Phys.* **72**, 2774 (1980).
- [11] E. Kretschmann and H. Raether, Radiative decay of non radiative surface plasmons excited by light, *Z. Naturforsch. A* **23**, 2135 (1968).
- [12] K. Takatori, T. Okamoto, K. Ishibashi, and R. Micheletto, Surface exciton polaritons supported by a J-aggregate-dye/air interface at room temperature, *Opt. Lett.* **42**, 3876 (2017).
- [13] M. C. Estevez, M. Alvarez, and L. M. Lechuga, Integrated optical devices for lab-on-a-chip biosensing applications, *Laser Photonics Rev.* **6**, 463 (2012).
- [14] J. N. Anker, W. P. Hall, O. Lyandres, N. C. Shah, J. Zhao, and R. P. Van Duyne, Biosensing with plasmonic nanosensors, *Nat. Mater.* **7**, 442 (2008).
- [15] J. Zhu, S. K. Ozdemir, Y.-F. Xiao, L. Li, L. He, D.-R. Chen, and L. Yang, On-chip single nanoparticle detection and sizing by mode splitting in an ultrahigh-Q microresonator, *Nat. Photonics* **4**, 46 (2010).
- [16] Y. Zhi, X.-C. Yu, Q. Gong, L. Yang, and Y.-F. Xiao, Single nanoparticle detection using optical microcavities, *Adv. Mater.* **29**, 1604920 (2017).
- [17] X. Fan, I. M. White, S. I. Shopova, H. Zhu, J. D. Suter, and Y. Sun, Sensitive optical biosensors for unlabeled targets: A review, *Anal. Chim. Acta* **620**, 8 (2008).
- [18] Y. Wang, W. Knoll, and J. Dostalek, Bacterial pathogen surface plasmon resonance biosensor advanced by long range surface plasmons and magnetic nanoparticle assays, *Anal. Chem.* **84**, 8345 (2012).
- [19] J.-F. Masson, Surface plasmon resonance clinical biosensors for medical diagnostics, *ACS Sens.* **2**, 16 (2017).
- [20] L. Zhou, Y. Cao, B. Lin, S. Song, Y. Yu, and L. Shui, In-situ visual and ultrasensitive detection of phosmet using a fluorescent immunoassay probe, *Sens. Actuators B Chem.* **241**, 915 (2017).
- [21] J. Liu, X. Zhou, Z. Qiao, J. Zhang, C. Zhang, T. Xiang, L. Shui, Y. Shi, and L. Liu, Integrated optical chemical sensor based on an SOI ring resonator using phase-interrogation, *IEEE Photonics J.* **6**, 6802207 (2014).
- [22] Y. Xu, L. Wu, and L. K. Ang, MoS<sub>2</sub>-based highly sensitive near-infrared surface plasmon resonance refractive index

- sensor, *IEEE J. Sel. Top. Quantum Electron.* **25**, 4600307 (2019).
- [23] Y. Xu, C.-Y. Hsieh, L. Wu, and L. Ang, Two-dimensional transition metal dichalcogenides mediated long range surface plasmon resonance biosensors, *J. Phys. D: Appl. Phys.* **52**, 065101 (2019).
- [24] Y. Xu, Y. S. Ang, L. Wu, and L. K. Ang, High sensitivity surface plasmon resonance sensor based on two-dimensional MXene and transition metal dichalcogenide: A theoretical study, *Nanomaterials* **9**, 165 (2019).
- [25] C.-T. Yang, Y. Xu, M. Pourhassan-Moghaddam, D. P. Tran, L. Wu, X. Zhou, and B. Thierry, Surface plasmon enhanced light scattering biosensing: Size dependence on the gold nanoparticle tag, *Sensors* **19**, 323 (2019).
- [26] Y. Xu, P. Bai, X. Zhou, Y. Akimov, C. E. Png, L.-K. Ang, W. Knoll, and L. Wu, Optical refractive index sensors with plasmonic and photonic structures: Promising and inconvenient truth, *Adv. Opt. Mater.* **7**, 1801433 (2019).
- [27] J. Homola, Surface plasmon resonance sensors for detection of chemical and biological species, *Chem. Rev.* **108**, 462 (2008).
- [28] K. M. Mayer and J. H. Hafner, Localized surface plasmon resonance sensors, *Chem. Rev.* **111**, 3828 (2011).
- [29] Q.-H. Phan, P.-M. Yang, and Y.-L. Lo, Surface plasmon resonance prism coupler for gas sensing based on stokes polarimetry, *Sens. Actuators B Chem.* **216**, 247 (2015).
- [30] M. Quan, J. Tian, and Y. Yao, Ultra-high sensitivity Fabry–Perot interferometer gas refractive index fiber sensor based on photonic crystal fiber and vernier effect, *Opt. Lett.* **40**, 4891 (2015).
- [31] F. Xing, Y. Yang, J. Shen, W. Jiang, Z. Liu, S. Zhu, and X. Yuan, Ultra-high sensitivity, multi-parameter monitoring of dynamical gas parameters using a reduced graphene oxide microcavity, *Sens. Actuators B Chem.* **235**, 474 (2016).
- [32] C.-Y. Chao, W. Fung, and L. J. Guo, Polymer microring resonators for biochemical sensing applications, *IEEE J. Sel. Top. Quantum Electron.* **12**, 134 (2006).
- [33] S. Grego, K. H. Gilchrist, J. B. Carlson, and B. R. Stoner, A compact and multichannel optical biosensor based on a wavelength interrogated input grating coupler, *Sens. Actuators B Chem.* **161**, 721 (2012).
- [34] S. Pham, M. Dijkstra, A. Hollink, L. Kauppinen, R. de Ridder, M. Pollnau, P. Lambeck, and H. Hoekstra, On-chip bulk-index concentration and direct, label-free protein sensing utilizing an optical grating-waveguide cavity, *Sens. Actuators B Chem.* **174**, 602 (2012).
- [35] M. Polyanskiy, Refractive index database, <http://refractive-index.info>.
- [36] P. B. Johnson and R. W. Christy, Optical constants of the noble metals, *Phys. Rev. B* **6**, 4370 (1972).
- [37] A. Shalabney and I. Abdulhalim, Electromagnetic fields distribution in multilayer thin film structures and the origin of sensitivity enhancement in surface plasmon resonance sensors, *Sens. Actuators A Phys.* **159**, 24 (2010).
- [38] S. V. Gaponenko, *Introduction to Nanophotonics* (Cambridge University Press, Cambridge, 2010).
- [39] See Supplemental Material at <http://link.aps.org/supplemental/10.1103/PhysRevApplied.12.024029> for additional data and descriptions.
- [40] Y. Akimov and L. Wu, Helmholtz decomposition analysis of electron energy loss: Differentiating resonances on polarization and radiation eigenmodes, *J. Opt. Soc. Am. B* **36**, 1472 (2019).
- [41] J. Ashley, Y. Shukor, R. D’Aurelio, L. Trinh, T. L. Rodgers, J. Temblay, M. Pleasants, and I. E. Tothill, Synthesis of molecularly imprinted polymer nanoparticles for  $\alpha$ -casein detection using surface plasmon resonance as a milk allergen sensor, *ACS Sens.* **3**, 418 (2018).
- [42] B. Chen, C. Liu, L. Ge, and K. Hayashi, Localized surface plasmon resonance gas sensor of Au nano-islands coated with molecularly imprinted polymer: Influence of polymer thickness on sensitivity and selectivity, *Sens. Actuators B Chem.* **231**, 787 (2016).
- [43] R. Verma and B. D. Gupta, Detection of heavy metal ions in contaminated water by surface plasmon resonance based optical fibre sensor using conducting polymer and chitosan, *Food Chem.* **166**, 568 (2015).
- [44] X.-Y. Xu, X.-G. Tian, L.-G. Cai, Z.-L. Xu, H.-T. Lei, H. Wang, and Y.-M. Sun, Molecularly imprinted polymer based surface plasmon resonance sensors for detection of sudan dyes, *Anal. Methods* **6**, 3751 (2014).
- [45] S. Jiang, Y. Peng, B. Ning, J. Bai, Y. Liu, N. Zhang, and Z. Gao, Surface plasmon resonance sensor based on molecularly imprinted polymer film for detection of histamine, *Sens. Actuators B Chem.* **221**, 15 (2015).
- [46] E. Makhneva, A. Obrušník, Z. Farka, P. Skládal, M. Vandebossche, D. Hegemann, and L. Zajíčková, Carboxyl-rich plasma polymer surfaces in surface plasmon resonance immunosensing, *Jpn. J. Appl. Phys.* **57**, 01AG06 (2017).